Medical Image Analysis 97 (2024) 103227

Contents lists available at ScienceDirect

Medical Image Analysis

journal homepage: www.elsevier.com/locate/media

Multi-detector fusion and Bayesian smoothing for tracking viral and chromatin structures

C. Ritter [a,*], J.-Y. Lee [b,d], M.-T. Pham [b,d], M.K. Pabba [c], M.C. Cardoso [c], R. Bartenschlager [b,d], K. Rohr [a]

[a] Biomedical Computer Vision Group, BioQuant, IPMB, Heidelberg University, Im Neuenheimer Feld 267, Heidelberg, Germany
[b] Department of Infectious Diseases, Molecular Virology, Heidelberg University, Im Neuenheimer Feld 344, Heidelberg, Germany
[c] Department of Biology, Cell Biology and Epigenetics, Technical University of Darmstadt, Schnittspahnstraße 10, Darmstadt, Germany
[d] German Center for Infection Research (DZIF), Heidelberg Partner Site, Germany

ARTICLE INFO

Keywords:
Biomedical imaging
Microscopy images
Particle detection and tracking
Multi-detector data fusion
Covariance intersection algorithm

ABSTRACT

Automatic tracking of viral and intracellular structures displayed as spots with varying sizes in fluorescence microscopy images is an important task to quantify cellular processes. We propose a novel probabilistic tracking approach for multiple particle tracking based on multi-detector and multi-scale data fusion as well as Bayesian smoothing. The approach integrates results from multiple detectors using a novel intensity-based covariance intersection method which takes into account information about the image intensities, positions, and uncertainties. The method ensures a consistent estimate of multiple fused particle detections and does not require an optimization step. Our probabilistic tracking approach performs data fusion of detections from classical and deep learning methods as well as exploits single-scale and multi-scale detections. In addition, we use Bayesian smoothing to fuse information of predictions from both past and future time points. We evaluated our approach using image data of the Particle Tracking Challenge and achieved state-of-the-art results or outperformed previous methods. Our method was also assessed on challenging live cell fluorescence microscopy image data of viral and cellular proteins expressed in hepatitis C virus-infected cells and chromatin structures in non-infected cells, acquired at different spatial–temporal resolutions. We found that the proposed approach outperforms existing methods.

1. Introduction

To understand and quantify cellular processes, intensive research is carried out using time-lapse fluorescence microscopy imaging and image analysis. Automatic detection and tracking of viral structures tagged with fluorescent labels is an important task to quantify virus infection processes and kinetics (Ewers et al., 2005; Arhel et al., 2006; Ivanchenko et al., 2009; Chang et al., 2011; Lee et al., 2019; Imle et al., 2019). Also, to characterize nuclear organization and chromatin motility (Heun et al., 2001; Levi and Gratton, 2008; Krawczyk et al., 2012), detection and tracking of fluorescently labeled chromatin structures is required. Due to the limited spatial resolution of optical microscopy, such structures have a spot-like appearance in the image data. The main steps of particle tracking are particle detection and association. Reliable detection and accurate localization of particles are important since errors are propagated to the association step and generally degrade the tracking performance. The main challenges for particle detection and tracking are low signal-to-noise ratio (SNR), small particle size, heterogeneity in particle size, high object density, lack of prominent particle shape, complex motion, and clutter.

1.1. Particle detection and tracking

Particle detection methods can be subdivided into single-scale and multi-scale approaches. Performance evaluations of different methods were carried out in Ruusuvuori et al. (2010), Smal et al. (2010) and Štěpka et al. (2015). *Single-scale* approaches exploit information from only one image scale (e.g., Bright and Steel, 1987; Breen et al., 1991; Thomann et al., 2002; Sage et al., 2005; Smal et al., 2008b; Pan et al., 2010; Rezatofighi et al., 2012). The spot-enhancing filter (SEF) (Sage et al., 2005) enhances particles while reducing noise and applies a Laplacian-of-Gaussian (LoG) filter. The standard deviation of the LoG needs to be adjusted according to the size of the particles. Model fitting approaches that fit Gaussian models to the image intensities (Thomann et al., 2002; Godinez et al., 2009; Pan et al., 2010) and detection

* Corresponding author.
E-mail addresses: christian.ritter@bioquant.uni-heidelberg.de (C. Ritter), k.rohr@uni-heidelberg.de (K. Rohr).

https://doi.org/10.1016/j.media.2024.103227
Received 8 July 2022; Received in revised form 15 August 2023; Accepted 27 May 2024
Available online 8 June 2024

approaches based on grayscale morphology using h-dome transformation were also proposed (Vincent, 1993; Smal et al., 2008b; Rezatofighi et al., 2012). These approaches assume a relatively simple appearance model of particles (Gaussian functions). Top-hat filters for particle detection (Bright and Steel, 1987; Breen et al., 1991) exploit the mean intensities in local neighborhoods. The size of the local neighborhoods needs to be adjusted according to the size of the particles. *Multi-scale* approaches use information from multiple image scales to detect particles with varying size (e.g., Olivo-Marin, 2002; Basset et al., 2015; Jaiswal et al., 2015; Gudla et al., 2017; Newby et al., 2018; Wollmann et al., 2019). Olivo-Marin (2002) proposed a detection method based on Wavelet transformation which employs wavelet multi-scale products. Jaiswal et al. (2015) proposed a multi-scale SEF approach (MSSEF) which iteratively exploits multiple scales. Basset et al. (2015) introduced ATLAS which is an adaptive thresholding scheme with autoselected scale selection. All these multi-scale detection approaches use only a single detection method. In recent years, deep learning approaches have been introduced for particle detection in microscopy images (Gudla et al., 2017; Newby et al., 2018; Wollmann et al., 2019). Approaches based on convolutional neural networks (CNNs) have been proposed (Gudla et al., 2017; Newby et al., 2018). These methods require a relatively large number of parameters or are based on a sliding window scheme. Wollmann et al. (2019) proposed an hourglass-shaped Deconvolution Network denoted as DetNet which has a significantly reduced number of parameters and does not require a sliding window scheme.

For *particle tracking*, different methods have been introduced and evaluated (e.g., Chenouard et al., 2014). The methods can be subdivided into deterministic, probabilistic, and deep learning approaches. *Deterministic* tracking approaches perform either particle detection and correspondence finding (e.g., Cox, 1993; Sbalzarini and Koumoutsakos, 2005; Jaqaman et al., 2008; Godinez et al., 2009) or obtain trajectories by finding minimal cost paths in a spatial–temporal volume (e.g., Bonneau et al., 2005; Xue and Leake, 2009). However, these approaches do not consider uncertainties, and suffer from erroneous detections or challenging object constellations for correspondence finding (e.g., clutter, spurious objects). *Probabilistic* tracking approaches take into account uncertainties and are based on a Bayesian framework where particle positions are determined from a posterior distribution incorporating noisy measurements (e.g., Genovesio et al., 2006; Smal et al., 2008a; Godinez and Rohr, 2015; Jaiswal et al., 2015; Roudot et al., 2017; Ritter et al., 2018; Dmitrieva et al., 2019; Ritter et al., 2021). Most Bayesian filtering methods exploit only two frames and only past information for correspondence finding in contrast to Bayesian smoothing approaches (Roudot et al., 2017; Ritter et al., 2018, 2021) which consider multiple frames by taking into account information from past and future time points. Roudot et al. (2017) introduced piecewise-stationary motion smoothing to cope with heterogeneous movements and use single measurements for Kalman filtering. In Ritter et al. (2018), a two-filter smoothing approach was proposed which exploits multiple measurements obtained from a single detector using probabilistic data association with elliptical sampling (PDAE) (Godinez and Rohr, 2015). Ritter et al. (2021) introduced a PDAE-based smoothing approach with multi-sensor data fusion (SMS-PDAE), which fuses predictions from both past and future time points by covariance intersection and integrates multiple measurements from a single detector. Coraluppi and Carthel (2011), Chenouard et al. (2013) and Liang et al. (2014) proposed multiple-hypothesis tracking approaches that explore the correspondence space over multiple time points which requires high computational cost and seek globally optimal solutions, but may not yield locally best assignments. In recent work, *deep learning* methods for particle tracking were introduced (e.g., Yao et al., 2020; Spilger et al., 2020, 2021) which use recurrent neural networks to determine assignment probabilities for correspondence finding. However, these methods require ground truth data for training and exploit only position information but not image intensity information. All existing particle tracking approaches use a single detection method.

1.2. Contributions

In this contribution, we introduce a novel probabilistic approach for particle tracking in fluorescence microscopy images based on *multi-detector multi-scale data fusion* and *Bayesian smoothing*. Our approach integrates multiple measurements (detections) from multiple detectors using multiple image scales by a novel *intensity-based covariance intersection* method. Covariance intersection is a data fusion method for unknown cross-covariances which ensures a consistent estimate. Existing covariance intersection methods are position-based, and were applied to synthetic and remote sensing images (Julier and Uhlmann, 2009; Guo et al., 2010; Deng et al., 2012) and microscopy images (Ritter et al., 2021). In comparison, the proposed intensity-based covariance intersection method exploits image intensities besides positions and uncertainties, and does not require an optimization step. In addition, we integrate detections from different methods, both classical and deep learning methods as well as exploit detections in multiple image scales. Further, for each particle a time-varying estimate of the measurement noise covariance is computed to improve update estimation. False positive detections are rejected using image likelihoods that represent the image intensities in the local neighborhood of detections. Information from future time points are integrated by Bayesian smoothing. We fuse predictions as well as motion information from past and future time points obtained by two filters running in opposite temporal directions.

The proposed approach for particle tracking is the first that integrates detections from multiple methods using multiple scales and performs Bayesian smoothing to integrate temporal information over time. We also introduce a novel intensity-based covariance intersection method for multi-detector multi-scale data fusion. Our approach has been evaluated using data from the Particle Tracking Challenge and yielded state-of-the-art results or better results than previous methods. Further, we performed a quantitative evaluation for challenging live cell time-lapse microscopy image data of different subcellular structures, namely viral and cellular proteins expressed in hepatitis C virus (HCV) infected cells and fluorescently labeled chromatin structures in non-infected cells, acquired at different spatial–temporal resolutions. Our approach obtained superior results compared to existing methods.

2. Methods

2.1. Overview of our approach

The proposed particle tracking approach integrates multiple measurements from multiple particle detectors within a Bayesian framework and combines multi-detector data fusion with Bayesian smoothing. Results from multiple detectors are fused by a novel intensity-based covariance intersection which ensures a consistent fused estimate of particle measurements and exploits image intensities, positions, and uncertainty information. Further, we incorporate information from past and future time points. Multiple detection-based and prediction-based measurements are generated by probabilistic data association with elliptical sampling (PDAE) (Godinez and Rohr, 2015) and are integrated in a Kalman filter-based tracking approach.

Below, we first describe particle tracking as Bayesian estimation problem. Then, we present our multi-detector data fusion approach by intensity-based covariance intersection. Subsequently, we describe the Bayesian smoothing approach for tracking which incorporates information from past and future time points.

2.2. Particle tracking by Bayesian filtering

We formulate particle tracking within a Bayesian framework where a particle at time point t is represented by a state vector $\mathbf{x}_t = (p_x, \dot{p}_x, p_y, \dot{p}_y, I_{\max}, \sigma_{xy})^T$ consisting of the position $\mathbf{p}_t = (p_x, p_y)^T$, velocity $\mathbf{v}_t = (\dot{p}_x, \dot{p}_y)^T$, and intensity information $\mathbf{I}_t = (I_{\max}, \sigma_{xy})^T$. $I_{\max}$ is the maximum intensity and σ_{xy} the width of a Gaussian appearance model

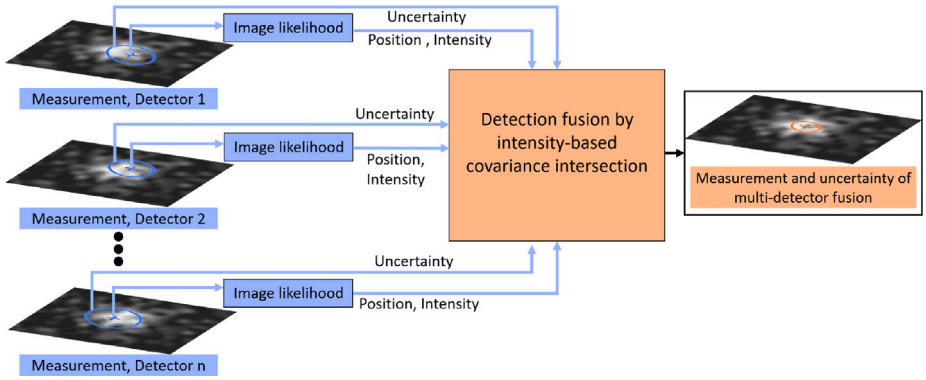

Fig. 1. Overview of our multi-detector intensity-based covariance intersection method (MD-iCI).

$g_{\text{Gauss}}(x, y; \mathbf{x}_t) = I_\text{b} + (I_\text{max} - I_\text{b}) \exp\left(-\frac{(x-p_x)^2+(y-p_y)^2}{2\sigma_{xy}^2}\right)$ with background intensity I_b. The dynamic model $p(\mathbf{x}_t|\mathbf{x}_{t-1})$ describes the temporal evolution of the state $\mathbf{x}_t$. To estimate $\mathbf{x}_t$, the noisy measurement $\mathbf{y}_t = (\overline{p}_x, \overline{p}_y, \overline{I}_\text{max}, \overline{\sigma}_{xy})^T$ is exploited by the measurement model $p(\mathbf{y}_t|\mathbf{x}_t)$, and a Bayesian filter (Särkkä, 2013) is used to determine the posterior distribution $p(\mathbf{x}_t|\mathbf{y}_{1:t})$ conditionally on all measurements $\mathbf{y}_{1:t} \in \mathbb{R}^{4\times t}$ up to time point t using Bayes' theorem

$$p(\mathbf{x}_t|\mathbf{y}_{1:t}) = \frac{p(\mathbf{y}_t|\mathbf{x}_t) \int p(\mathbf{x}_t|\mathbf{x}_{t-1})\ p(\mathbf{x}_{t-1}|\mathbf{y}_{1:t-1})\, \mathrm{d}\mathbf{x}_{t-1}}{\int p(\mathbf{y}_t|\mathbf{x}_t)\ p(\mathbf{x}_t|\mathbf{y}_{1:t-1})\, \mathrm{d}\mathbf{x}_t} \tag{1}$$

The posterior distribution $p(\mathbf{x}_t|\mathbf{y}_{1:t}) \sim \mathcal{N}(\mathbf{x}_t; \mathbf{m}_t, \mathbf{P}_t)$ with mean $\mathbf{m}_t \in \mathbb{R}^{6\times 1}$ and covariance matrix $\mathbf{P}_t \in \mathbb{R}^{6\times 6}$ can be calculated in a closed form via the Kalman filter if linear and Gaussian models are assumed for the dynamic model and the measurement model:

$$p(\mathbf{x}_t|\mathbf{x}_{t-1}) \sim \mathcal{N}(\mathbf{x}_t; \mathbf{F}\,\mathbf{m}_{t-1}, \mathbf{Q}) \tag{2}$$

$$p(\mathbf{y}_t|\mathbf{x}_t) \sim \mathcal{N}(\mathbf{y}_t; \mathbf{H}\,\mathbf{m}_t, \mathbf{R}) \tag{3}$$

For $p(\mathbf{x}_t|\mathbf{x}_{t-1})$, a random walk model with $\mathbf{F} = \text{diag}(1,1,1,1,1,1)$ is assumed and the covariance matrix $\mathbf{Q} = \text{diag}(q_{p_x}, q_{\dot{p}_x}, q_{p_y}, q_{\dot{p}_y}, q_{I_\text{max}}, q_{\sigma_{xy}})$ reflects the uncertainty of the dynamic model. For $p(\mathbf{y}_t|\mathbf{x}_t)$, a measurement model $\mathbf{y}_t = \mathbf{H}\,\mathbf{m}_t$ is used and the uncertainty is reflected by the covariance matrix $\mathbf{R} = \text{diag}(r_{p_x}, r_{p_y}, r_{I_\text{max}}, r_{\sigma_{xy}})$. Based on the state estimate $\mathbf{x}_{t-1}$, the mean $\hat{\mathbf{m}}_t$ and covariance $\hat{\mathbf{P}}_t$ of the predicted state $\hat{\mathbf{x}}_t$ are computed by

$$\hat{\mathbf{m}}_t = \mathbf{F}\,\mathbf{m}_{t-1} \tag{4}$$

$$\hat{\mathbf{P}}_t = \mathbf{F}\,\mathbf{P}_{t-1}\,\mathbf{F}^T + \mathbf{Q} \tag{5}$$

Using the prediction, the mean $\mathbf{m}_t$ and covariance $\mathbf{P}_t$ of the state $\mathbf{x}_t$ is given by

$$\mathbf{m}_t = \hat{\mathbf{m}}_t + \mathbf{K}_t\,(\mathbf{y}_t - \mathbf{H}\,\hat{\mathbf{m}}_t) \tag{6}$$

$$\mathbf{P}_t = (\mathbf{I} - \mathbf{K}_t\,\mathbf{H})\,\hat{\mathbf{P}}_t \tag{7}$$

where $\mathbf{I} \in \mathbb{R}^{6\times 6}$ is the identity matrix and $\mathbf{K}_t \in \mathbb{R}^{6\times 4}$ is the Kalman gain $\mathbf{K}_t = \hat{\mathbf{P}}_t\,\mathbf{H}^T\left(\mathbf{H}\,\hat{\mathbf{P}}_t\,\mathbf{H}^T + \mathbf{R}\right)^{-1}$.

2.3. Multi-detector fusion

Probabilistic particle tracking approaches based on Bayesian filtering often use the Kalman filter and exploit *single measurements* for prediction and update estimation (e.g., Genovesio et al., 2006; Chenouard et al., 2013; Roudot et al., 2017). *Multiple measurements* (via elliptical sampling around the detection and prediction) were used in the probabilistic data association with elliptical sampling (PDAE) approach (Godinez and Rohr, 2015). The Smoothing Multi-Sensor PDAE (SMS-PDAE) approach (Ritter et al., 2021) integrates multiple measurements and exploits separate uncertainties to improve update estimation. However, PDAE and SMS-PDAE employ a *single* detection method and use a *single* image scale. In contrast, the proposed tracking approach integrates detections from *multiple* methods (with *separate* uncertainties) and uses *multiple* image scales to improve measurement and update estimation. Particles are detected by different methods and the detections are fused to reduce the overall uncertainty and increase the accuracy. A consistent fused estimate can be obtained by the covariance intersection (CI) algorithm (Julier and Uhlmann, 1997), which determines the optimal weighting coefficients of each detection on the fused result. However, an iterative optimization scheme is required and intensity information is not used. We suggest a different approach, where the calculation of weighting coefficients by optimization is replaced by computing image likelihoods directly from the image intensities. The proposed intensity-based covariance intersection (iCI) approach for multi-detector (MD) data fusion is denoted by MD-iCI and takes into account image intensities, positions, and uncertainties from multiple detectors. An overview is given in Fig. 1.

For each detector $i \in \{1, 2, \ldots, n\}$ at time point t, a measurement $\mathbf{y}_{i,t} \in \mathbb{R}^{4\times 1}$ with uncertainty $\mathbf{R}_i \in \mathbb{R}^{4\times 4}$ is obtained. The fused measurement $\mathbf{y}_{\text{f},t} \in \mathbb{R}^{4\times 1}$ at time point t (corresponding to one object in an image) can be determined by the unbiased linear combination of the measurements $\mathbf{y}_{i,t}$ (Julier and Uhlmann, 1997)

$$\mathbf{y}_{f,t} = \sum_{i=1}^{n} \mathbf{K}_i\,\mathbf{y}_{i,t} \tag{8}$$

with the gain matrices $\mathbf{K}_i \in \mathbb{R}^{4\times 4}$. The $\mathbf{K}_i$ are determined by optimizing a cost function $J(\mathbf{R}_\text{f})$ of the covariance matrix $\mathbf{R}_\text{f} \in \mathbb{R}^{4\times 4}$ of the fused measurement

$$\mathbf{R}_\text{f} = \begin{bmatrix}\mathbf{K}_1 & \cdots & \mathbf{K}_n\end{bmatrix}\begin{bmatrix}\mathbf{R}_1^1 & \cdots & \mathbf{R}_1^n \\ \vdots & \ddots & \vdots \\ \mathbf{R}_n^1 & \cdots & \mathbf{R}_n^n\end{bmatrix}\begin{bmatrix}\mathbf{K}_1 \\ \vdots \\ \mathbf{K}_n\end{bmatrix} \tag{9}$$

with $\sum_{i=1}^{n} \mathbf{K}_i = \mathbf{I}$, and $\mathbf{I}$ is the identity matrix. $J(\mathbf{R}_\text{f})$ is a strictly monotonically increasing function such as the trace or determinant of $\mathbf{R}_\text{f}$ (Reinhardt et al., 2015; Chen et al., 2002; Niehsen, 2002). The matrices $\mathbf{R}_i^i$ in (9) represent the covariances of measurement $\mathbf{y}_{i,t}$, and the matrices $\mathbf{R}_i^j$ represent the cross-covariances of measurement $\mathbf{y}_{i,t}$ from detector i based on the measurement $\mathbf{y}_{j,t}$ from detector j.

2.3.1. Multi-detector fusion with intensity-based covariance intersection (MD-iCI)

In our MD-iCI, all detectors are applied to the same image. Therefore, the measurement errors can be assumed to be correlated due to common image noise, and the measurement processes are not independent, i.e. the cross-covariances in (9) are not zero ($\mathbf{R}_i^j \neq \mathbf{0}$ for $i \neq j$) and *unknown*. Fusing multiple measurements $\mathbf{y}_{i,t}$, a *consistent* estimate of the fused measurement $\mathbf{y}_{\text{f},t}$ is represented by the ellipsoid corresponding to the fused covariance matrix $\mathbf{R}_\text{f}$ which bounds the intersection of all ellipsoids of $\mathbf{R}_i^j$ (Julier and Uhlmann, 1997; Reinhardt et al., 2015). An estimate is consistent if it converges to the true parameter and

the covariance of the estimation error converges to zero as the sample number increases. Using the CI algorithm (Julier and Uhlmann, 1997; Niehsen, 2002), the intersection for unknown cross-covariances can be characterized by a convex combination of the covariances and allows computing an optimal fused measurement

$$\mathbf{y}_{\mathrm{f},t} = \mathbf{R}_{\mathrm{f,t}} \sum_{i=1}^{n} \omega_i \left(\mathbf{R}_i\right)^{-1} \mathbf{y}_{i,t} \qquad \mathbf{R}_{\mathrm{f,t}} = \left(\sum_{i=1}^{n} \omega_i \left(\mathbf{R}_i\right)^{-1}\right)^{-1} \tag{10}$$

$$0 \leq \omega_i \leq 1 \quad \text{and} \quad \sum_{i=1}^{n} \omega_i = 1$$

Existing CI algorithms (e.g., Julier and Uhlmann, 2009; Deng et al., 2012) are *position-based* (i.e. they use the positions of detections) and determine the optimal weighting coefficients ω_i by minimizing the trace (or determinant) of $\mathbf{R}_{\mathrm{f}}$ with respect to ω_i (Reinhardt et al., 2015). However, this is a nonlinear optimization problem with constraints, which requires high computation costs (Deng et al., 2012). Also, intensity information is not exploited. In contrast, we suggest a different approach to compute ω_i by exploiting image intensities besides positions and uncertainties. Since the weighting coefficients are constrained to $\omega_i \in [0,1]$ and $\sum_{i=1}^{n} \omega_i = 1$, we interpret them as probabilities. We propose using the probabilities of how well the image intensities within a region-of-interest (ROI) around each detection $\mathbf{y}_{i,t}$ represent particle intensities synthesized with the used Gaussian appearance model (cf. Section 2.2). The probabilities are computed based on the image likelihood which was previously used in Godinez and Rohr (2015) for computing association weights to solve correspondence finding. Instead, we here use the probabilities based on the image likelihood to incorporate information of the image intensities around the position $\overline{\mathbf{p}}_{i,t} = (\overline{p}_x, \overline{p}_y)$ of $\mathbf{y}_{i,t}$ to determine the *intensity-based* weighting coefficients for fusing detections. The image likelihood α_i is defined by

$$\alpha_i = \frac{p_o\left(I_{\mathrm{ROI}}\left(\overline{\mathbf{p}}_{i,t}\right) | I_{g_{\mathrm{Gauss}}}\left(\overline{\mathbf{p}}_{i,t}\right)\right)}{p_b\left(I_{\mathrm{ROI}}\left(\overline{\mathbf{p}}_{i,t}\right) | I_{I_b}\left(\overline{\mathbf{p}}_{i,t}\right)\right)} \tag{11}$$

where $p_o(\cdot)$ is the image object likelihood defined as the Euclidean distance between the image intensities within the ROI around $\overline{\mathbf{p}}_{i,t}$ and the image intensities synthesized with the Gaussian appearance model of a particle. $p_b(\cdot)$ is the background image likelihood which is defined analogously using the ROI background value I_b. Since we interpret the weighting coefficients as probabilities, we use the normalization

$$\omega_i = \frac{\alpha_i}{\sum_{i=1}^{n} \alpha_i} \tag{12}$$

Thus, since the constraints for ω_i of the existing CI algorithms in (10) are fullfilled, our MD-iCI yields a consistent estimate. This was proofed in Julier and Uhlmann (1997) for arbitrary weighting coefficients. MD-iCI determines the fused measurement $\mathbf{y}_{\mathrm{f},t}$ using the computed intensity-based ω_i and incorporates uncertainties by the covariance matrices $\mathbf{R}_i$ of measurements $\mathbf{y}_{i,t}$ by

$$\mathbf{y}_{\mathrm{f},t} = \mathbf{R}_{\mathrm{f,t}} \sum_{i=1}^{n} \left(\frac{\alpha_i}{\sum_{i=1}^{n} \alpha_i}\right) \left(\mathbf{R}_i\right)^{-1} \mathbf{y}_{i,t} \tag{13}$$

The ω_i are computed for each time point t, thus the fused measurement covariance matrix

$$\mathbf{R}_{\mathrm{f,t}} = \left(\sum_{i=1}^{n} \left(\frac{\alpha_i}{\sum_{i=1}^{n} \alpha_i}\right) \left(\mathbf{R}_i\right)^{-1}\right)^{-1} \tag{14}$$

is changing over time and is a *time-varying* estimate of the measurement noise covariance. In contrast, previous probabilistic tracking approaches (e.g., Genovesio et al., 2006; Godinez et al., 2009; Coraluppi and Carthel, 2011; Jaiswal et al., 2015; Godinez and Rohr, 2015; Roudot et al., 2017; Ritter et al., 2021) used a fixed measurement covariance matrix or an uncorrelated matrix (white Gaussian noise), and did not exploit image intensity to determine the measurement noise.

2.3.2. Measurement rejection and assignment

In our MD-iCI, we use the image likelihood α_i in (11) to identify false positive detections and reject them from fusion. The α_i quantify how well the intensities around measurement $\mathbf{y}_{i,t}$ from detector i agree with the intensities of a particle synthesized with the Gaussian appearance model (cf. Section 2.2). If α_i is below a threshold, $\mathbf{y}_{i,t}$ is classified as false positive detection and rejected for fusion (see Fig. 2 for an example). When applying N_d detectors to an image with multiple particles, each detector yields a set of detections. For time point t, the detector with the largest number of detections is identified and a one-to-one correspondence with detections from the other detectors is found by a global nearest neighbor method based on a graph-theoretical approach for the transportation problem (Sbalzarini and Koumoutsakos, 2005). We use the detector with the largest number of detections to obtain the maximum number of one-to-one correspondences. Next, among the $N_d - 1$ detectors with unassigned detections, the detector with the largest number of detections is identified and one-to-one correspondences between detections are determined. This sequential procedure is completed after maximum $N_d - 1$ iterations and the remaining unassigned detections are used for track initialization.

2.4. Bayesian smoothing for tracking

Our MD-iCI approach uses spatial information from multiple detectors. For tracking, we also exploit temporal information using Bayesian smoothing and incorporate past and future time points. We denote our tracking approach as multi-detector Bayesian smoothing (MD-BS). An overview of MD-BS is shown in Fig. 3. The posterior probability distribution $p\left(\mathbf{x}_t | \mathbf{y}_{\mathrm{f},1:T}\right)$ is computed conditionally on all fused measurements $\mathbf{y}_{\mathrm{f},1:T} \in \mathbb{R}^{4\times T}$ up to time point T, where $T > t$ is a future time point (Särkkä, 2013):

$$p\left(\mathbf{x}_t | \mathbf{y}_{\mathrm{f},1:T}\right) = p\left(\mathbf{x}_t | \mathbf{y}_{\mathrm{f},1:t}\right) \int \frac{p\left(\mathbf{x}_{t+1} | \mathbf{x}_t\right)\, p\left(\mathbf{x}_{t+1} | \mathbf{y}_{\mathrm{f},1:T}\right)}{p\left(\mathbf{x}_{t+1} | \mathbf{y}_{\mathrm{f},1:t}\right)} \mathrm{d}\mathbf{x}_{t+1} \tag{15}$$

We solve (15) by using two MS-PDAE (Multi-Sensor PDAE, Ritter et al. (2021)) in conjunction with the proposed MD-iCI running forward and backward in time analogously to the two-filter smoothing approach by Fraser and Potter (1969). At time point t, forward tracking provides a predicted state $\hat{\mathbf{x}}_{t|t-1} \in \mathbb{R}^{6\times 1}$ based on the state at time point $t-1$ due to the Markovian property (Särkkä, 2013). Analogously, backward tracking provides a predicted state $\hat{\mathbf{x}}_{t|t+1} \in \mathbb{R}^{6\times 1}$ based on the state at time point $t+1$. The two predicted states are fused as described below.

2.4.1. Prediction fusion with covariance intersection algorithm

Our MD-BS computes the state $\mathbf{x}_t$ based on the fused predicted state $\hat{\mathbf{x}}_{\mathrm{f},t}$ determined from the forward predicted state $\hat{\mathbf{x}}_{t|t-1}$ and the backward predicted state $\hat{\mathbf{x}}_{t|t+1}$. Two filters are running forward and backward in time and both use the same motion and noise model. Thus, the estimation errors of $\hat{\mathbf{x}}_{t|t-1}$ and $\hat{\mathbf{x}}_{t|t+1}$ are correlated due to common noise models (Bar-Shalom and Campo, 1986; Bar-Shalom, 1981). Further, the cross-covariances $\hat{\mathbf{P}}_{t|t-1\,;\,t|t+1}$ and $\hat{\mathbf{P}}_{t|t+1\,;\,t|t-1}$ are not zero and *unknown*. In this case, a *consistent* estimate of $\hat{\mathbf{x}}_{\mathrm{f},t}$ with mean $\hat{\mathbf{m}}_{\mathrm{f},t}$ and covariance $\hat{\mathbf{P}}_{\mathrm{f},t}$ can be obtained by the CI algorithm (Julier and Uhlmann, 1997):

$$\hat{\mathbf{m}}_{\mathrm{f},t} = \hat{\mathbf{P}}_{\mathrm{f},t} \left[\omega \left(\hat{\mathbf{P}}_{t|t-1}\right)^{-1} \hat{\mathbf{m}}_{t|t-1} + (1-\omega) \left(\hat{\mathbf{P}}_{t|t+1}\right)^{-1} \hat{\mathbf{m}}_{t|t+1}\right] \tag{16}$$

$$\hat{\mathbf{P}}_{\mathrm{f},t} = \left[\omega \left(\hat{\mathbf{P}}_{t|t-1}\right)^{-1} + (1-\omega) \left(\hat{\mathbf{P}}_{t|t+1}\right)^{-1}\right]^{-1} \tag{17}$$

where $\hat{\mathbf{m}}_{t|t-1}$ and $\hat{\mathbf{m}}_{t|t+1}$ are the mean of the predicted states $\hat{\mathbf{x}}_{t|t-1}$ and $\hat{\mathbf{x}}_{t|t+1}$, respectively. In the MD-BS, we equally weight the information from the forward and backward filters using $\omega = 0.5$. Note that the prediction is a coarse estimate of the position of a particle and generally not exactly located at a particle. Thus, exploiting intensity information at the predicted position generally does not improve the result. $\hat{\mathbf{x}}_{t|t-1}$ and $\hat{\mathbf{x}}_{t|t+1}$ are assigned by a global nearest neighbor method (Sbalzarini and Koumoutsakos, 2005).

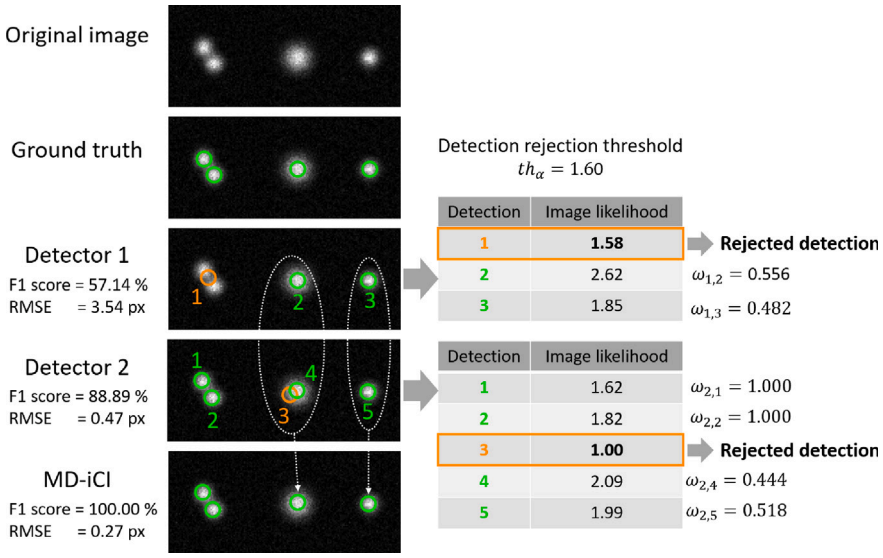

Fig. 2. MD-iCI and measurement rejection for synthetic data. Ground truth and MD-iCI detections are shown by green circles. For detector 1 and 2, orange circles represent false positive and rejected detections, green circles represent detections used by MD-iCI, and the corresponding table shows the image likelihood and weighting coefficients. The white dotted ellipses depict assigned and fused detections by MD-iCI. Detector 1 is sensitive for large particles leading to a false positive detection for two small particles located close together. Detector 2 is sensitive to small particles and yields a false positive detection for the large particle. MD-iCI fuses the detections of detector 1 and 2 and obtains the best F1 score and $RMSE$ compared to the single detectors.

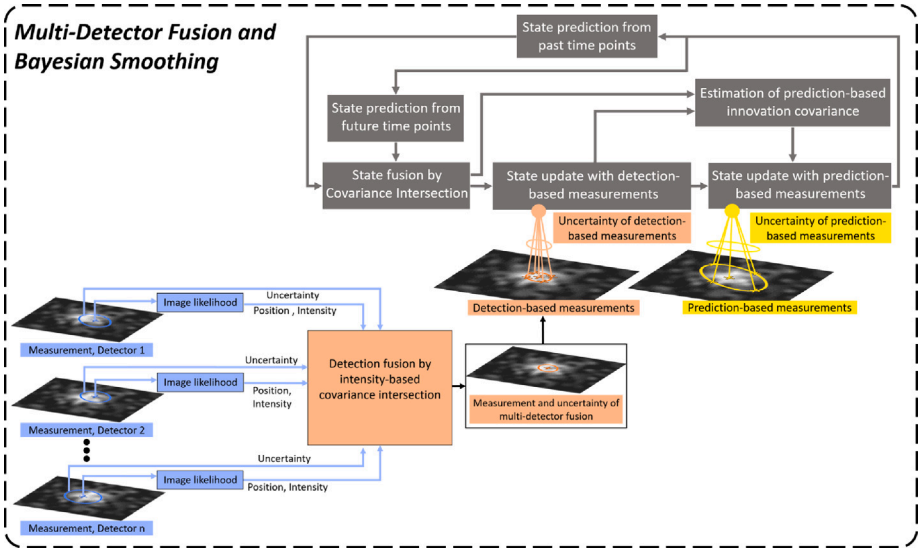

Fig. 3. Overview of our MD-BS tracking approach. The approach combines our MD-iCI for multi-detector fusion (spatial information) and Bayesian smoothing with covariance intersection for prediction fusion (temporal information).

2.4.2. *Multi-sensor PDAE with multi-detector fusion*

MD-BS uses forward and backward MS-PDAE filters in conjunction with MD-iCI. Both MS-PDAE filters exploit multiple measurements by generating detection-based and prediction-based measurements within local elliptical regions around the detections and predictions. The two different measurement processes have separate uncertainties and the multiple measurements are integrated by a sequential multi-sensor data fusion approach consisting of two steps to determine the state $\mathbf{x}_t$.

First, the state $\mathbf{x}_{\text{Det},t} \in \mathbb{R}^{6\times1}$ (with mean $\mathbf{m}_{\text{Det},t} \in \mathbb{R}^{6\times1}$ and covariance matrix $\mathbf{P}_{\text{Det,t}} \in \mathbb{R}^{6\times6}$) is determined using the fused predicted state $\hat{\mathbf{x}}_{\text{f},t}$ (with mean $\hat{\mathbf{m}}_{\text{f},t}$ and covariance matrix $\hat{\mathbf{P}}_{\text{f},t}$) and the *detection-based* measurements $\mathbf{y}_{\text{f},i,\text{Det},t}$ by computing

$$\mathbf{m}_{\text{Det},t} = \hat{\mathbf{m}}_{\text{f,t}} + \mathbf{K}_{\text{Det},t}\,\mathbf{v}_{\text{Det},t} \tag{18}$$

$$\mathbf{P}_{\text{Det,t}} = \left(\mathbf{I} - \mathbf{K}_{\text{Det},t}\,\mathbf{H}\right)\hat{\mathbf{P}}_{\text{f},t} \tag{19}$$

where $\mathbf{v}_{\text{Det},t} = \sum_{i=1}^{N_{\text{Det}}} \beta_{i,\text{Det},t}\,\mathbf{v}_{i,\text{Det},t}$ is the combined innovation consisting of the association probabilities $\beta_{i,\text{Det},t} \in [0,1]$ (based on a Gaussian appearance model for spot-like particles, see Section 2.2) and the innovations $\mathbf{v}_{i,\text{Det},t} = \mathbf{y}_{\text{f},i,\text{Det},t} - \mathbf{H}\,\hat{\mathbf{m}}_t$. $\mathbf{y}_{\text{f},i,\text{Det},t}$ are determined within elliptical regions around the fused detection $\mathbf{y}_{\text{f},t}$ obtained by our MD-iCI. The Kalman gain matrix for $\mathbf{y}_{\text{f},i,\text{Det},t}$ is given by:

$$\mathbf{K}_{\text{Det},t} = \hat{\mathbf{P}}_{\text{f},t}\,\mathbf{H}^T\left(\mathbf{S}_{\text{Det},t}\right)^{-1} \tag{20}$$

$$\mathbf{S}_{\text{Det},t} = \mathbf{H}\,\hat{\mathbf{P}}_{\text{f},t}\,\mathbf{H}^T + \mathbf{R}_{\text{f,Det},t} \tag{21}$$

The innovation covariance matrix $\mathbf{S}_{\text{Det},t} \in \mathbb{R}^{4\times4}$ reflects the uncertainty of the innovation $\mathbf{v}_{\text{Det},t}$ and the uncertainty of $\mathbf{y}_{\text{f},i,\text{Det},t}$ is represented by the covariance matrix $\mathbf{R}_{\text{f,Det},t} \in \mathbb{R}^{4\times4}$ obtained by MD-iCI. Note that the covariance matrix $\mathbf{R}_{\text{f,Det},t}$ is changing over time in contrast to Ritter et al. (2021) where a fixed covariance matrix was used.

Second, the state $\mathbf{x}_t$ (with mean $\mathbf{m}_t$ and covariance matrix $\mathbf{P}_t$) is determined by the estimate $\mathbf{x}_{\text{Det},t}$ (with mean $\mathbf{m}_{\text{Det},t}$ and covariance

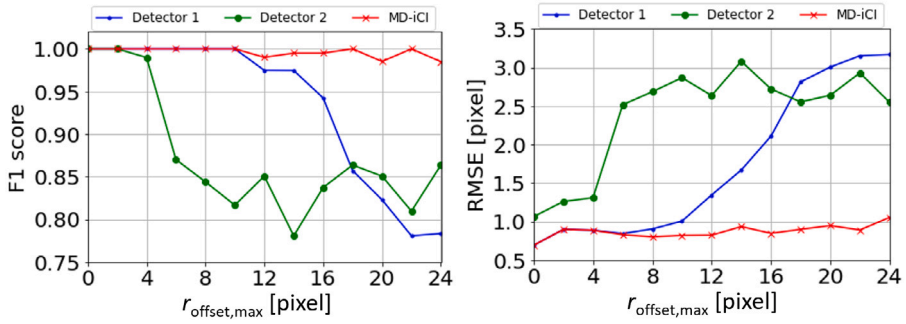

(a) Detection performance (b) Localization performance

Fig. 4. Performance of MD-iCI (red curve) compared to two SEFs with $\sigma_{\text{LoG}} = 3.0$ (blue) and $\sigma_{\text{LoG}} = 8.0$ (green) for images with increasing $r_{\text{offset, max}}$ (maximum particle radii offsets) corresponding to increasing particle size heterogeneity. MD-iCI fuses the detections of the two SEFs. (a) Detection performance by the F1 score. (b) Localization performance by $RMSE$.

matrix $\mathbf{P}_{\text{Det,t}}$) and the *prediction-based* measurements $\mathbf{y}_{j,\text{Pred},t}$ with

$$\mathbf{m}_t = \mathbf{m}_{\text{Det},t} + \mathbf{K}_{\text{Pred},t}\,\mathbf{v}_{\text{Pred},t} \tag{22}$$

$$\mathbf{P}_t = \left(\mathbf{I} - \mathbf{K}_{\text{Pred},t}\,\mathbf{H}\right)\mathbf{P}_{\text{Det},t} \tag{23}$$

where $\mathbf{v}_{\text{Pred},t} = \sum_{j=1}^{N_{\text{Pred}}} \beta_{j,\text{Pred},t}\,\mathbf{v}_{j,\text{Pred},t}$ is the combined innovation with the association probabilities $\beta_{j,\text{Pred},t} \in [0,1]$ (based on a Gaussian appearance model) and the innovations $\mathbf{v}_{j,\text{Pred},t} = \mathbf{y}_{j,\text{Pred},t} - \mathbf{H}\,\mathbf{m}_{\text{Det},t}$. The Kalman gain matrix for $\mathbf{y}_{j,\text{Pred},t}$ is given by:

$$\mathbf{K}_{\text{Pred},t} = \mathbf{P}_{\text{Det},t}\,\mathbf{H}^T\left(\mathbf{H}\,\mathbf{P}_{\text{Det},t}\,\mathbf{H}^T + \mathbf{H}\,\hat{\mathbf{P}}_{\text{f},t}\,\mathbf{H}^T\right)^{-1} \tag{24}$$

The detection-based measurements $\mathbf{y}_{\text{f},i,\text{Det},t}$ are determined within an elliptical sampling region centered at the position of the fused detection obtained by MD-iCI. The prediction-based measurements $\mathbf{y}_{j,\text{Pred},t}$ are obtained analogously using the position of the predicted state.

For the assignment between predictions and measurements, we use a displacement-based correspondence finding approach (Ritter et al., 2021), which exploits motion information from past and future time points. We employ displacements obtained by the two MS-PDAE with MD-iCI running in opposite temporal directions and use a graph-theoretical approach (Sbalzarini and Koumoutsakos, 2005) to solve the correspondence problem.

3. Experimental results

We evaluated the detection and localization performance of the proposed multi-detector fusion approach with intensity-based covariance intersection (MD-iCI) and studied the tracking performance of the proposed probabilistic approach based on multi-detector data fusion and Bayesian smoothing (MD-BS). We used data of the Particle Tracking Challenge (Chenouard et al., 2014) as well as different time-lapse fluorescence microscopy images of hepatitis C virus associated proteins and chromatin structures.

3.1. Synthetic data

We assessed the detection and localization performance of MD-iCI on synthetic image data showing particles with heterogeneous size. We generated synthetic images with 512 × 512 pixels that display 100 particles represented by a 2D Gaussian function. For each image, a particle has a radius (standard deviation of the 2D Gaussian function) between $r_{\min}$ and $r_{\max}$, sampled from a uniform distribution. For $r_{\min}$ we used 4 pixels, while $r_{\max} = r_{\min} + r_{\text{offset, max}}$ and $r_{\text{offset, max}}$ varies for the different images (from 0 to 24 pixels) and defines the variation of particle sizes (heterogeneity) in an image. To simulate camera noise (e.g., CCD) the images are corrupted by Poisson noise (Sbalzarini and Koumoutsakos, 2005).

We compared MD-iCI with two different single-scale spot-enhancing filters (SEF) (Sage et al., 2005). SEF uses a Laplacian-of-Gaussian (LoG) filter with standard deviation σ_{LoG} followed by thresholding. The threshold is determined by the mean of the absolute values of the filter responses plus a factor c times the standard deviation. This method is often used for particle detection.

The detection performance is quantified by the F1 score $\in [0,1]$, where a value of 1 represents a perfect result. The localization performance is quantified by the mean $RMSE \in [0,5]$ between detected particles and ground truth. The assignment between detected particles and ground truth was determined by the Munkres algorithm (Kuhn, 1955) with a maximal gating distance of 5 pixels. To compare the detection approaches, we considered the $RMSE$ of true positive as well as false negative detections. This has the advantage that the number of considered detections is the same for all methods. If a ground truth particle is not matched with a computed detection, a localization error of 5 pixels (maximal gating distance) is used.

First, we studied images with an increasing $r_{\text{offset, max}}$ (maximum particle radii offset) from 0 to 24 pixels. We used SNR = 1.89. The detection performance is shown in Fig. 4a and the localization performance is displayed in Fig. 4b. It turns out, that MD-iCI performs best. MD-iCI yields for all images an F1 score above 98% compared to two single-scale SEFs ($\sigma_{\text{LoG}} = 3.0$ and 8.0) which obtain F1 scores above 78%. MD-iCI yields for all images an $RMSE$ below 1.1 pixels, whereas both SEFs obtain $RMSE$s up to 3.08 and 3.17 pixels. An example detection result is shown in Fig. 5 for $r_{\text{offset, max}} = 16$ pixels (yielding particle radii between 4 and 20 pixels). It can be seen, that MD-iCI detects all particles with various sizes compared to both SEFs.

Second, we considered different SNR levels (SNR = 1 to 7) and used $r_{\text{offset, max}} = 12$ pixels as well as $r_{\text{offset, max}} = 16$ pixels. The result is shown in Fig. 6. For both $r_{\text{offset, max}}$, MD-iCI yields for all SNR levels an F1 score above 97% and an $RMSE$ below 1.4 pixels. In contrast, the first SEF (with $\sigma_{\text{LoG}} = 3.0$) obtains an F1 score above 90% for $r_{\text{offset, max}} = 12$ pixels, and above 78% for $r_{\text{offset, max}} = 16$ pixels. The second SEF ($\sigma_{\text{LoG}} = 8.0$) yields an F1 score above 78% both $r_{\text{offset, max}}$. Further, the first SEF yields an $RMSE$ below 2.5 pixels for $r_{\text{offset, max}} = 12$ pixels and below 3.4 pixels for $r_{\text{offset, max}} = 16$, whereas the second SEF yields an $RMSE$ below 3.1 pixels for both $r_{\text{offset, max}}$. It also turns out that for a larger $r_{\text{offset, max}}$ (larger size heterogeneity) the performance of the SEFs is reduced while the performance of MD-iCI is not affected.

3.2. Particle Tracking Challenge data

We assessed our multi-detector fusion approach MD-iCI and our tracking approach MD-BS on image data from the Particle Tracking Challenge (Chenouard et al., 2014). We used time-lapse image sequences of the vesicle scenario with all object densities and all low

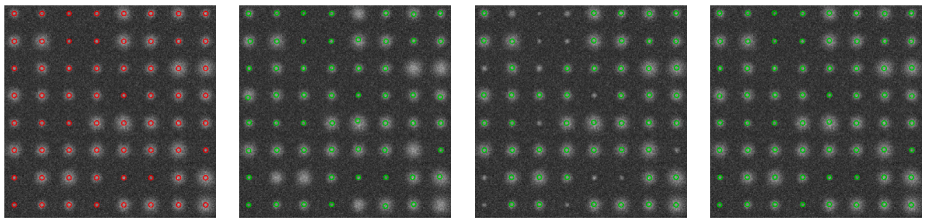

(a) Ground truth (b) SEF ($\sigma_{\mathrm{LoG}} = 3.0$) (c) SEF ($\sigma_{\mathrm{LoG}} = 8.0$) (d) MD-iCI

Fig. 5. Ground truth and detection results for two SEFs ($\sigma_{\mathrm{LoG}} = 3.0$ and $\sigma_{\mathrm{LoG}} = 8.0$) and MD-iCI for a synthetic image with $r_{\mathrm{offset,\ max}} = 16$ pixels. Only MD-iCI correctly detects all particles.

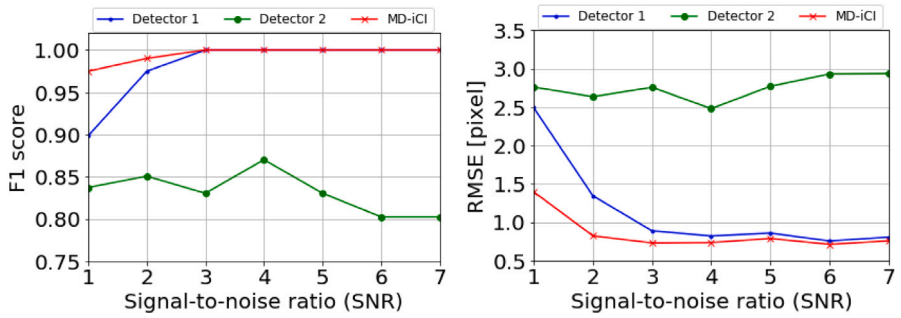

(a) $r_{\mathrm{offset,\ max}} = 12$ pixels

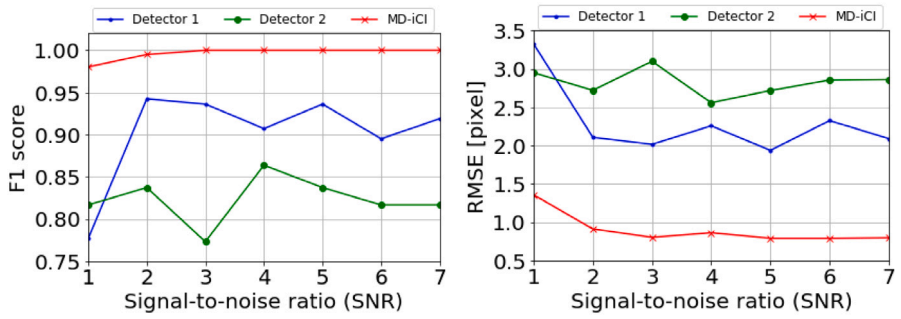

(b) $r_{\mathrm{offset,\ max}} = 16$ pixels

Fig. 6. Performance of MD-iCI (red curve) compared to two SEFs with $\sigma_{\mathrm{LoG}} = 3.0$ (blue) and $\sigma_{\mathrm{LoG}} = 8.0$ (green) for images with different SNR levels for (a) $r_{\mathrm{offset,\ max}} = 12$ and (b) $r_{\mathrm{offset,\ max}} = 16$ pixels.

SNR levels. We selected the vesicle scenario since this dataset shows particles with random motion which is the dominant motion type of viral and chromatin structures as considered in our applications using fluorescence live cell microscopy image sequences (Section 3.3). Also, the structures have a more or less round shape compared to elongated shapes in the microtubule scenario of the Particle Tracking Challenge. We focus on low SNR levels, since it is known from previous studies that these SNR levels are challenging for particle detection and tracking (Chenouard et al., 2014). The number of particles ranges from around 100 for low object density to around 1000 for high object density. Each of the six image sequences consists of 100 images with 512×512 pixels.

For particle detection and localization, we compared MD-iCI with two single-scale SEFs (Sage et al., 2005). For SEF 1 we used a standard deviation $\sigma_{\mathrm{LoG}} = 3$ pixels for low and medium object density as well as for high object density and SNR = 1, and we employed $\sigma_{\mathrm{LoG}} = 2$ pixels for high object density and SNR = 2. For SEF 2 we used $\sigma_{\mathrm{LoG}} = 4$ pixels for low object density, $\sigma_{\mathrm{LoG}} = 2$ pixels for medium object density, and $\sigma_{\mathrm{LoG}} = 4$ pixels for high object density and SNR = 1 and $\sigma_{\mathrm{LoG}} = 2$ pixels for SNR = 2. These parameter choices yielded the best result. Besides the classical method SEF, we also compared MD-iCI with the multi-scale deep learning method DetNet (Wollmann et al., 2019). DetNet is an adapted Deconvolution Network which naturally handles objects at multiple scales by the hourglass-shape of the network. For each image sequence, we used the last image for training DetNet and the first image for validation. We investigated two variants of MD-iCI, one which fuses the detections of two SEFs (MD-iCI 1) and one which fuses the detections of DetNet and two SEFs (MD-iCI 2).

The detection performance is quantified by the F1 score $\in [0, 1]$ computed as the mean F1 score over all images of a sequence. The localization performance is quantified by the mean $RMSE \in [0, 5]$ (cf. Section 3.1). The assignment between detected particles and ground truth was determined by the Munkres algorithm (Kuhn, 1955) with a maximal gating distance of 5 pixels. The detection performance for all object densities and all SNR levels is shown in Table 1, and the best performing method is marked in bold. MD-iCI 2 outperforms the other methods for SNR = 1 for all object densities, and for SNR = 2 for the challenging high and medium density. For SNR = 2 and low density, DetNet yields the best result. Further, MD-iCI 1 performs better for all SNR levels and all object densities than the single-scale SEFs. The localization performance is given in Table 2. MD-iCI 2 obtains the best localization results for all SNR levels and all object densities. Further, MD-iCI 1 yields better localization results compared to both single-scale SEFs for all SNR levels and all object densities, and performs better than DetNet for all SNR levels and low object density.

Table 1
Detection performance for all object densities for low SNR levels for the Particle Tracking Challenge data in terms of the F1 score [%].

Seq.	SEF 1	SEF 2	DetNet	MD-iCI 1	MD-iCI 2
SNR = 1					
Low	26.06	18.53	25.90	26.19	**26.82**
Medium	36.55	21.18	49.75	38.68	**50.42**
High	38.40	34.82	48.56	44.61	**55.79**
SNR = 2					
Low	79.96	72.50	**90.18**	80.08	82.49
Medium	80.82	78.33	90.61	85.74	**90.94**
High	79.27	81.69	84.76	86.40	**87.39**
Mean	56.84	51.18	64.96	60.28	**65.64**
Std. dev.	11.51	13.20	12.19	11.99	**11.37**

Table 2
Localization performance for all object densities for low SNR levels for the Particle Tracking Challenge data in terms of the $RMSE$.

Seq.	SEF 1	SEF 2	DetNet	MD-iCI 1	MD-iCI 2
SNR = 1					
Low	4.38	4.76	4.67	4.37	**4.36**
Medium	4.43	4.70	4.24	4.36	**4.15**
High	4.42	4.52	4.24	4.30	**4.00**
SNR = 2					
Low	2.29	3.37	2.40	2.28	**2.16**
Medium	2.93	3.03	2.45	2.55	**2.23**
High	2.99	2.92	2.84	2.54	**2.47**
Mean	3.57	3.88	3.47	3.40	**3.23**
Std. dev.	0.42	**0.39**	0.46	0.46	0.47

Table 3
Mean performance metrics over all object densities for low SNR levels for the Particle Tracking Challenge data.

Metric	α	β	JSC_θ	JSC	$RMSE$
Method 5	0.327	0.275	0.523	0.365	1.752
Method 1	0.176	0.130	0.278	0.154	**1.281**
Method 2	0.345	0.261	0.479	0.350	1.899
SMS-PDAE	0.338	0.288	**0.527**	0.376	1.674
MD-BS 1	0.351	0.293	0.526	0.391	1.695
MD-BS 2	**0.360**	**0.296**	0.523	**0.404**	1.833

For particle tracking, we performed a comparison of MD-BS with the overall top-three performing methods (Method 5, 1, 2) of the Particle Tracking Challenge. Method 5 uses SEF for particle detection and PDAE for particle linking (Godinez and Rohr, 2015). Method 1 employs iterative centroid calculation for particle localization and assigns particles by combinatorial optimization (Sbalzarini and Koumoutsakos, 2005). Method 2 detects particles by convolution with a disk shaped object and finds correspondences by multiple-hypothesis tracking (Coraluppi and Carthel, 2011). We also compared MD-BS with the recent SMS-PDAE method (Ritter et al., 2021). SMS-PDAE uses SEF for particle detection and temporal multi-sensor data fusion with covariance intersection for tracking. For SMS-PDAE and Method 5 we used SEF 1, since it yielded a better detection and localization performance than SEF 2 (cf. Tables 1 and 2). We investigated two variants of MD-BS, one which fuses the detections of two SEFs (SEF 1 and SEF 2) denoted as MD-BS 1 and one which fuses the detections of DetNet and two SEFs (SEF 1 and SEF 2) denoted as MD-BS 2.

The tracking performance is evaluated by the metrics α, β, JSC_θ, JSC, and $RMSE$ from the Particle Tracking Challenge (Chenouard et al., 2014). α and β quantify association and localization errors. $\alpha \in [0,1]$ provides the overall matching quality between ground truth and computed trajectories where a perfect matching is given by $\alpha = 1$ and no matching is reflected by $\alpha = 0$. $\beta \in [0,\alpha]$ considers additionally spurious trajectories compared to α. The similarity at the track level is evaluated by the Jaccard similarity coefficient $JSC_\theta \in [0,1]$. The Jaccard similarity coefficient $JSC \in [0,1]$ quantifies the detection performance, and the root mean-square error $RMSE$ evaluates the localization performance. Table 3 shows the mean values of all tracking performance metrics over all object densities and all low SNR levels. MD-BS 2 outperforms all methods for three out of five metrics, namely α, β, and JSC. Further, MD-BS 1 shows improved results for α, β, and JSC compared to SMS-PDAE and Method 5. The results for individual SNR levels and individual object densities are provided in Appendix. In Fig. 7, three example trajectories for SNR = 2 and medium object density for different tracking approaches are shown. Only MD-BS (we used MD-BS 2) yields three complete trajectories. By fusing multiple detection results and exploiting information from both past and future time points, MD-BS is able to obtain three complete trajectories (orange, blue, and purple). The other approaches yield one complete trajectory (orange), but other trajectories are not complete (blue) or are missing (purple).

3.3. Evaluation on time-lapse fluorescence microscopy images

We also evaluated our detection approach MD-iCI and our tracking approach MD-BS on challenging time-lapse microscopy data sets of viral and cellular proteins expressed in hepatitis C virus (HCV) infected cells and chromatin structures in non-infected cells. The images were acquired with confocal fluorescence microscopes using different spatial–temporal resolutions. In total, we used nine live cell microscopy image sequences and compared the results for object detection and localization as well as for tracking with those of previous methods.

3.3.1. HCV live cell confocal microscopy images

We applied our MD-iCI to three live cell microscopy image sequences displaying HCV-infected cells with mCherry-labeled host cell protein ApoE, mCherry-labeled viral protein NS5A, or mTurquoise2-labeled ApoE, respectively (Lee et al., 2019). The first two image sequences consist of 34 images with 225 × 194 and 177 × 249 pixels. The spatial resolution is 220 nm/pixel and the temporal resolution is 37 s/frame and 1.5 s/frame, respectively. The third image sequence consists of 91 images with 726 × 396 pixels. The spatial resolution is 90 nm/pixel and the temporal resolution is 2 s/frame. The image data was acquired with a PerkinElmer UltraVIEW ERS or VoX spinning disk confocal microscope mounted on a Nikon TE2000-E or TiE. The data is challenging due to heterogeneous object size, clutter, high object density, and complex motion.

For particle detection and localization, we performed a comparison of MD-iCI with SEF (Sage et al., 2005) and DetNet (Wollmann et al., 2019). For SEF we used two variants with different values for σ_{LoG}. For SEF 1 we used $\sigma_{\mathrm{LoG}} = 2$ pixels for all videos, and for SEF 2 we used $\sigma_{\mathrm{LoG}} = 2.6$ pixels for the first two videos and $\sigma_{\mathrm{LoG}} = 3$ pixels for the third video. These parameter choices yielded the best result. We trained DetNet on the last image of a video and used the first image for validation. Testing was done on the fifth image of a video. Further, we investigated two variants of MD-iCI, one which fuses detections of two SEFs (MD-iCI 1) and one which fuses the detections of DetNet and two SEFs (MD-iCI 2).

For the detection performance, we computed the F1 score $\in [0,1]$ for time point five for each image sequence. The localization performance is evaluated by the mean $RMSE \in [0,5]$ between detected particles and ground truth (cf. Section 3.1). The assignment between detected particles and ground truth was determined by the Munkres algorithm (Kuhn, 1955) with a maximal gating distance of 5 pixels. Each image sequence contains between 157 and 194 ground truth detections manually annotated using the Manual Tracking plug-in in ImageJ (Schneider et al., 2012). The detection performance is shown in Table 4 and the localization results are given in Table 5. For both detection and localization, MD-iCI 2 yields the best results for all three image sequences. Further, MD-iCI 1 outperforms both single-scale SEFs.

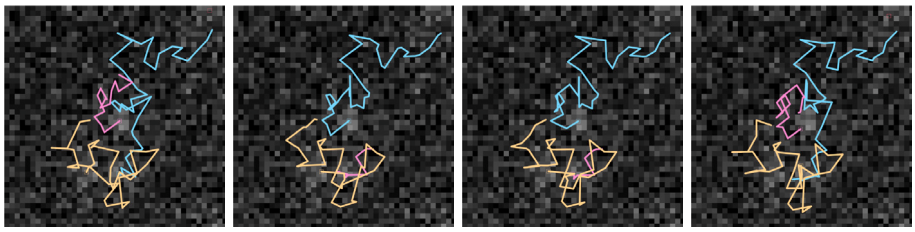

(a) Ground truth (b) PDAE (c) SMS-PDAE (d) MD-BS

Fig. 7. Ground truth and tracking results for different methods for the vesicle scenario from the Particle Tracking Challenge data with SNR = 2 and medium density (time point $t = 70$). Only MD-BS yields three complete trajectories.

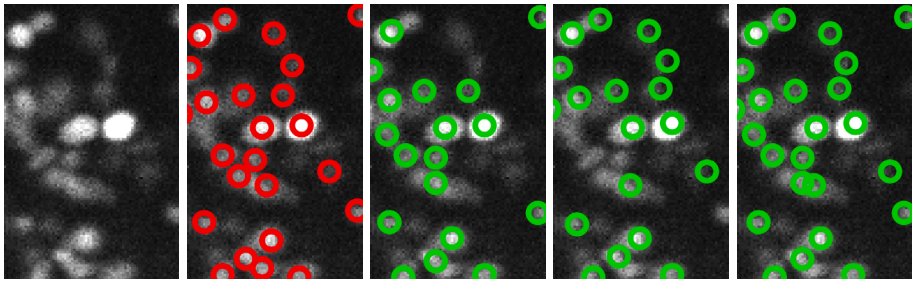

(a) Original image (b) Ground truth (c) SEF 2 (d) DetNet (e) MD-iCI

Fig. 8. Original image and detection results for HCV live cell microscopy data of fluorescently labeled ApoE proteins (time point $t = 5$).

Table 4
Detection results for HCV live cell image sequences, F1 score [%].

Seq.	SEF 1	SEF 2	DetNet	MD-iCI 1	MD-iCI 2
1	75.40	39.00	82.35	77.50	**83.38**
2	56.63	3.75	66.67	57.14	**69.83**
3	69.84	78.62	81.48	75.24	**84.08**
Mean	67.29	40.46	76.83	69.96	**79.10**
Std. dev.	6.82	26.49	6.23	7.89	**5.68**

Table 5
Localization results for HCV live cell image sequences, $RMSE$.

Seq.	SEF 1	SEF 2	DetNet	MD-iCI 1	MD-iCI 2
1	3.21	4.37	2.93	3.10	**2.71**
2	3.63	4.95	3.55	3.62	**2.64**
3	3.23	3.25	3.36	3.08	**2.90**
Mean	3.36	4.19	3.28	3.27	**2.75**
Std. dev.	0.17	0.61	0.22	0.22	**0.10**

Example detection results for MD-iCI 2 are displayed in Fig. 8 which show that our approach yields better results than SEF and DetNet.

For tracking of particles, we performed a comparison of MD-BS with a Kalman filter tracking approach (KF) (Tinevez et al., 2017), the ParticleTracker (PT) (Sbalzarini and Koumoutsakos, 2005), a multiple-hypothesis tracking approach (MHT) (de Chaumont et al., 2012; Chenouard et al., 2014), and the Smoothing Multi-Sensor PDAE (SMS-PDAE) (Ritter et al., 2021). KF uses an LoG filter for particle detection and linear assignment for correspondence finding. PT employs intensity-weighted centroid calculation for particle localization and assigns particles by combinatorial optimization. MHT localizes particles by a wavelet-based detection scheme and uses a Kalman filter with multiple motion models. SMS-PDAE employs a single-scale SEF, and we used SEF 1 since it yielded better results than SEF 2 (cf. Tables 4 and 5). We also investigated two variants of MD-BS, one which fuses the detections of two SEFs (SEF 1 and SEF 2) denoted as MD-BS 1 and one which fuses the detections of DetNet and two SEFs (SEF 1 and SEF 2) denoted as MD-BS 2.

Table 6
Tracking accuracy for HCV live cell image sequences, P_{track} [%].

Seq.	1	2	3	Mean	Std. dev.
KF	41.14	40.03	48.93	43.57	3.43
PT	30.88	33.35	29.22	31.15	**1.47**
MHT	61.46	72.32	41.51	58.43	11.05
SMS-PDAE	69.35	74.67	51.68	65.23	8.51
MD-BS 1	70.00	75.10	52.74	65.95	8.29
MD-BS 2	**70.25**	**77.34**	**54.42**	**67.34**	8.30

The tracking accuracy is evaluated by the measure $P_{\text{track}} \in [0, 1]$:

$$P_{\text{track}} = \frac{n_{\text{track,correct}}}{n_{\text{track,total}}} \tag{25}$$

$n_{\text{track,total}}$ is the number of ground truth trajectories and $n_{\text{track,correct}}$ the number of correctly computed trajectories. $n_{\text{track,correct}}$ is determined as Gaussian weighted sum of the percentage of correctly tracked time steps of a ground truth trajectory. The argument of the Gaussian weighting function (mean value 1, standard deviation 1) is the number of computed trajectories corresponding to a ground truth trajectory (ideally the number is one). The weighting penalizes broken computed trajectories (the larger the number of broken trajectories, the lower the weight). Correspondences between computed and ground truth trajectories are determined by a nearest neighbor approach with a maximal gating distance of 5 pixels (Godinez and Rohr, 2015). Ground truth was obtained by manual annotation using the Manual Tracking plug-in in ImageJ (29, 32, and 108 trajectories for the different videos). The number of objects in the images is about 100. Since manual annotation is not feasible for a large number of objects in a large number of image frames, only a certain number of objects were annotated for each image sequence. Since for the metrics of the Particle Tracking Challenge, ground truth for all objects in all frames of an image sequence is required, we used the performance metric P_{track}. The results are shown in Table 6. We also determined the mean P_{track} value as a measure of the overall performance. It turned out, that MD-BS 2 yields the best result for all image sequences and achieves a mean P_{track} of 67.34%. MD-BS 1 is somewhat worse and obtains better results than SMS-PDAE for all image sequences. In Fig. 9, example results are shown. MD-BS 2

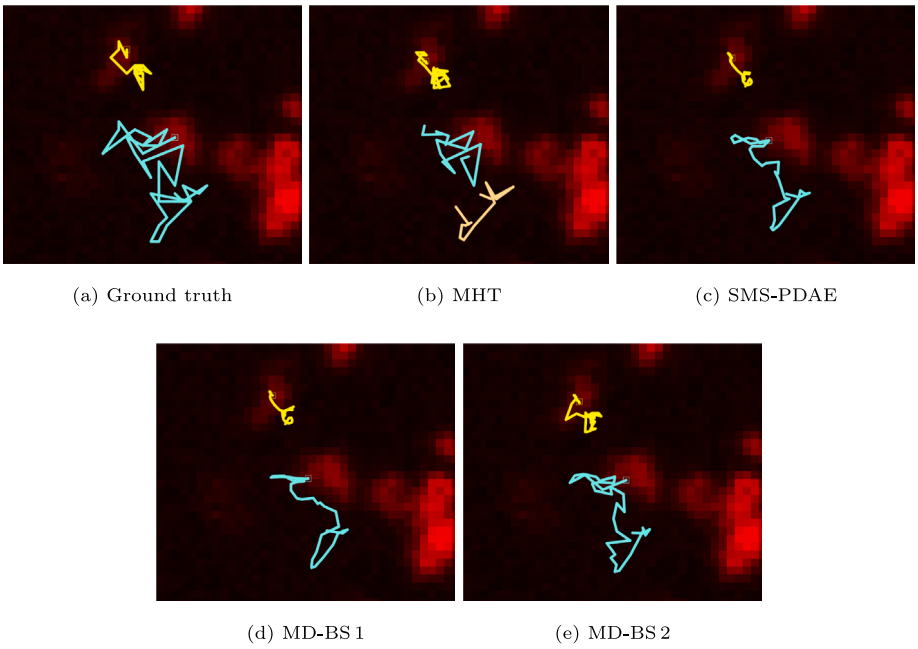

(a) Ground truth (b) MHT (c) SMS-PDAE

(d) MD-BS 1 (e) MD-BS 2

Fig. 9. Ground truth and tracking results for different methods for HCV live cell confocal microscopy images of fluorescently labeled ApoE proteins (time point $t = 34$).

yields more complete and correct trajectories than SMS-PDAE and MD-BS 1. MHT obtains a broken trajectory.

3.3.2. Chromatin live cell confocal microscopy images

We also evaluated MD-iCI and MD-BS using six challenging live cell microscopy image sequences with fluorescently labeled chromatin structures of HeLa Kyoto cells (Pabba et al., 2023). The image sequences consist of 63 images with 512 × 512 pixels. The spatial resolution is 48 nm/pixel for four videos, and 31 nm/pixel and 49 nm/pixel for the remaining videos. The temporal resolution is 0.985 s/frame for all videos. The images were acquired with a PerkinElmer UltraVIEW VoX confocal microscope. The data is challenging due to high heterogeneity in object size, high object density, and low SNR.

For chromatin detection and localization, we performed a comparison of MD-iCI with SEF and DetNet. For SEF we used two different variants, SEF 1 with $\sigma_{\text{LoG}} = 2.7$ pixels for all videos, and SEF 2 with $\sigma_{\text{LoG}} = 3.5$ pixels for two videos (videos 3 and 6) and $\sigma_{\text{LoG}} = 3$ pixels for the remaining videos. For DetNet, we randomly split the data into three videos for training, two for validation, and one for testing. For training we used the last image of a video, and for validation the first image. Testing was done on the first image of a video. We assessed two variants of MD-iCI as for the HCV data above. The results are given in Table 7. It turned out that MD-iCI 2 outperforms the other methods for all image sequences and obtains a mean F1 score of 83.67%. MD-iCI 1 performs better than both single-scale SEFs and obtains a mean F1 score of 78.92% compared to SEF 1 with 75.77% and SEF 2 with 61.50%. DetNet and MD-iCI 2 yield the lowest standard deviation for the F1 score (highest robustness). The localization performance is given in Table 8. MD-iCI 2 outperforms all methods for five out of six videos. MD-iCI 1 obtains the best result for one video and better results than both single-scale SEFs for all videos.

For chromatin tracking, we compared MD-BS with the same methods as for the HCV data above (Section 3.3.1). We manually annotated for each image sequence between 20 and 22 ground truth trajectories. The tracking results for all approaches are shown in Table 9. MD-BS 2 outperforms all other methods for all image sequences and achieves a mean P_{track} of 45.63%. MD-BS 1 obtains for all image sequences a better result than SMS-PDAE. Example detection results of MD-iCI 2 and tracking results of MD-BS 2 are shown in Fig. 10. It can be seen, that the detections are close to the ground truth for the challenging data with heterogeneous object size and that complete trajectories are obtained.

Table 7
Detection results for chromatin live cell image sequences, F1 score [%].

Seq.	SEF 1	SEF 2	DetNet	MD-iCI 1	MD-iCI 2
1	82.18	83.08	85.71	82.35	**86.49**
2	82.19	75.76	88.31	86.84	**89.74**
3	87.80	64.00	89.60	89.60	**91.34**
4	72.09	70.11	76.36	78.35	**79.30**
5	63.67	31.63	79.60	64.78	**80.67**
6	66.67	44.44	74.07	71.58	**74.47**
Mean	75.77	61.50	82.28	78.92	**83.67**
Std. dev.	9.69	8.79	**6.50**	9.41	6.58

Table 8
Localization results for chromatin live cell image sequences, $RMSE$.

Seq.	SEF 1	SEF 2	DetNet	MD-iCI 1	MD-iCI 2
1	2.58	2.70	2.29	2.55	**1.89**
2	2.94	3.31	2.36	2.60	**2.19**
3	2.67	3.71	2.39	2.46	**2.22**
4	3.40	3.47	2.95	2.96	**2.69**
5	3.77	4.55	3.09	3.73	**3.01**
6	3.33	4.04	3.26	**2.64**	2.72
Mean	3.12	3.63	2.72	2.82	**2.45**
Std. dev.	1.04	**0.28**	0.95	1.06	0.94

Table 9
Tracking accuracy for chromatin live cell image sequences, P_{track} [%].

Seq.	1	2	3	4	5	6	Mean	Std. dev.
KF	22.01	23.47	35.39	11.23	23.74	24.50	23.39	**7.68**
PT	39.68	24.76	31.09	6.37	36.99	20.00	26.48	12.29
MHT	38.06	26.87	48.87	24.30	40.99	42.64	36.96	9.53
SMS-PDAE	47.85	30.16	49.60	13.29	44.67	30.31	35.98	14.02
MD-BS 1	48.71	36.98	49.85	22.37	46.85	38.12	40.48	10.41
MD-BS 2	**53.94**	**47.21**	**55.64**	**24.44**	**49.72**	**42.80**	**45.63**	11.36

4. Conclusion

We introduced a novel probabilistic particle tracking approach based on multi-detector data fusion and Bayesian smoothing (MD-BS). We also proposed a novel intensity-based covariance intersection method (MD-iCI) which integrates multiple measurements by fusing

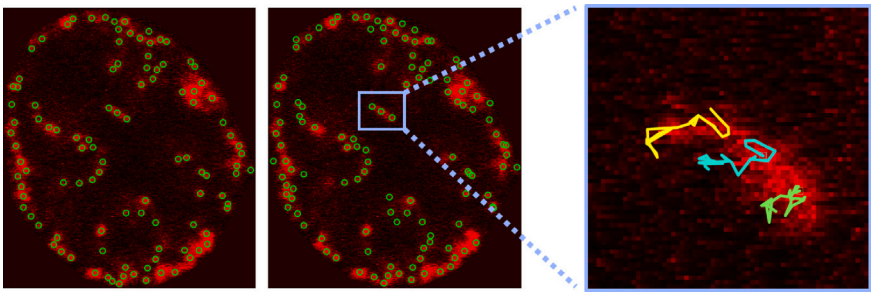

Fig. 10. Results for chromatin live cell microscopy data. (Left) Detection results of MD-iCI 2 (time point $t = 5$). (Right) Tracking results of MD-BS 2 for a region-of-interest (time point $t = 25$).

detections from multiple detectors in multiple image scales. MD-iCI exploits image intensities, positions, and uncertainties, and provides consistent estimates. Compared to existing covariance intersection algorithms, image intensities are exploited based on image likelihoods and an optimization step is not required. Further, a time-varying measurement noise covariance matrix is estimated for each particle to improve update estimation for particle tracking. False positive detections are rejected using image likelihoods in the local neighborhood of detections. Our MD-BS tracking method combines Bayesian smoothing with covariance intersection to fuse predictions from past and future time points obtained by two filters running in opposite temporal directions. In addition, motion information based on fused displacements from past and future time points is used to improve correspondence finding.

We quantitatively evaluated MD-BS using data from the Particle Tracking Challenge and obtained state-of-the-art results or outperformed previous methods. We also demonstrated that MD-iCI improves particle detection and localization compared to existing detection methods. In addition, we benchmarked MD-BS and MD-iCI on nine challenging live cell fluorescence microscopy image sequences acquired with microscopes using different spatial–temporal resolutions, and different types of subcellular structures. We found, that our approach outperforms previous methods for microscopy data of HCV associated proteins and chromatin structures including high object density, low SNR, heterogeneous object size, and complex motion.

In future work, our approach will be applied to other live cell fluorescence microscopy images of viral and chromatin structures to quantify viral kinetics and motility of intracellular structures to reveal new insights on viral and cellular processes.

Declaration of competing interest

The authors declare that they have no known competing financial interests or personal relationships that could have appeared to influence the work reported in this paper.

Data availability

Data will be made available on request.

Acknowledgments

This work has been funded by the Deutsche Forschungsgemeinschaft (DFG, German Research Foundation) - Project-ID 240245660 - SFB 1129 (projects Z4, P11), the SPP 2202 (RO 2471/10-1, CA 198/15-1, Project-ID 422831194) and (RO 2471/13-1, CA 198/20-1, Project-ID 529989072), and the SPP 2389. J.-Y. Lee and R. Bartenschlager acknowledge support by DZIF (TTU 05.712, project number 8029705712) and the Infectious Diseases Imaging Platform, headed by Vibor Laketa, at the CIID, Heidelberg, Germany.

Appendix. Performance values for low SNR levels and all object densities for the Particle Tracking Challenge data

The individual performance values for the low SNR levels SNR = 1 and 2 for all object densities (low, medium, high) are given in Tables A.1 and A.2 for all investigated methods for the vesicle scenario from the Particle Tracking Challenge data (Chenouard et al., 2014).

For SNR = 1, MD-BS 2 (two SEFs and DetNet) performs best for α, β, and JSC for medium object density, and outperforms all methods for α for the challenging high object density. Further, MD-BS 2 obtains better results for β and JSC than Methods 5, 1, and 2 for all object densities. MD-BS 1 (two SEFs) yields better results for α than SMS-PDAE for all object densities.

For SNR = 2, MD-BS 2 outperforms all methods for β and JSC for all object densities. For medium and low object density, MD-BS 2 performs best for JSC_θ, and for high object density it performs best for α. Further, MD-BS 2 obtains better results for β and JSC than Methods 5, 1, and 2 for all object densities. MD-BS 1 yields improved results for α, β, and JSC_θ compared to SMS-PDAE for all object densities.

Table A.1
Tracking performance for all object densities for SNR = 1 for the Particle Tracking Challenge data.

Metric	α	β	JSC_θ	JSC	$RMSE$
Low					
Method 5	0.211	0.112	0.185	0.179	2.119
Method 1	0.022	0.018	0.115	0.024	**1.568**
Method 2	0.175	0.104	**0.281**	0.178	2.423
SMS-PDAE	0.213	**0.130**	0.222	**0.206**	2.093
MD-BS 1	**0.225**	0.128	0.205	0.202	2.098
MD-BS 2	0.222	0.123	0.202	0.200	2.173
Medium					
Method 5	0.162	0.142	0.458	0.225	2.172
Method 1	0.027	0.026	0.300	0.034	**1.533**
Method 2	**0.198**	0.111	0.335	0.192	2.386
SMS-PDAE	0.171	0.152	**0.460**	0.239	2.083
MD-BS 1	0.180	0.152	0.438	0.240	2.130
MD-BS 2	**0.198**	**0.157**	0.440	**0.269**	2.387
High					
Method 5	0.136	0.120	0.460	0.198	2.296
Method 1	0.091	0.064	0.231	0.089	**1.859**
Method 2	0.163	0.080	0.324	0.147	2.531
SMS-PDAE	0.147	0.133	**0.464**	0.218	2.243
MD-BS 1	0.159	**0.134**	0.459	**0.227**	2.362
MD-BS 2	**0.181**	0.127	0.410	0.223	2.453

Table A.2
Tracking performance for all object densities for SNR = 2 for the Particle Tracking Challenge data.

Metric	α	β	JSC_θ	JSC	$RMSE$
Low					
Method 5	0.652	0.590	0.763	0.717	1.118
Method 1	0.225	0.155	0.232	0.178	**0.796**
Method 2	0.661	0.607	0.792	0.742	1.219
SMS-PDAE	0.668	0.612	0.777	0.724	0.991
MD-BS 1	**0.673**	0.613	0.778	0.772	0.982
MD-BS 2	0.671	**0.625**	**0.793**	**0.777**	1.198
Medium					
Method 5	0.448	0.391	0.664	0.489	1.325
Method 1	0.398	0.298	0.411	0.340	**0.840**
Method 2	**0.517**	0.417	0.629	0.510	1.254
SMS-PDAE	0.461	0.402	0.659	0.492	1.226
MD-BS 1	0.501	0.429	0.682	0.520	1.237
MD-BS 2	0.505	**0.440**	**0.706**	**0.553**	1.301
High					
Method 5	0.353	0.295	**0.607**	0.382	1.484
Method 1	0.294	0.217	0.379	0.256	**1.088**
Method 2	0.356	0.249	0.515	0.331	1.582
SMS-PDAE	0.365	0.299	0.577	0.378	1.405
MD-BS 1	0.368	0.303	0.591	0.385	1.362
MD-BS 2	**0.380**	**0.305**	0.587	**0.401**	1.488

References

Arhel, N., Genovesio, A., Kim, K.-A., Miko, S., Perret, E., Olivo-Marin, J.-C., Shorte, S., Charneau, P., 2006. Quantitative four-dimensional tracking of cytoplasmic and nuclear HIV-1 complexes. Nature Methods 3 (10), 817–824.

Bar-Shalom, Y., 1981. On the track-to-track correlation problem. IEEE Trans. Autom. Control 26 (2), 571–572.

Bar-Shalom, Y., Campo, L., 1986. The effect of the common process noise on the two-sensor fused-track covariance. IEEE Trans. Aerosp. Electron. Syst. AES-22 (6), 803–805.

Basset, A., Boulanger, J., Salamero, J., Bouthemy, P., Kervrann, C., 2015. Adaptive spot detection with optimal scale selection in fluorescence microscopy images. IEEE Trans. Image Process. 24 (11), 4512–4527.

Bonneau, S., Dahan, M., Cohen, L.D., 2005. Single quantum dot tracking based on perceptual grouping using minimal paths in a spatiotemporal volume. IEEE Trans. Image Process. 14 (9), 1384–1395.

Breen, E., Joss, G., Williams, K., 1991. Locating objects of interest within biological images: The top hat box filter. J. Comput.-Assist. Microsc. 3, 97–102.

Bright, D.S., Steel, E.B., 1987. Two-dimensional top hat filter for extracting spots and spheres from digital images. J. Microsc. 146 (2), 191–200.

Chang, L., Godinez, W.J., Kim, I.-H., Tektonidis, M., De Lanerolle, P., Eils, R., Rohr, K., Knipe, D.M., 2011. Herpesviral replication compartments move and coalesce at nuclear speckles to enhance export of viral late mRNA. Proc. Natl. Acad. Sci. USA 108 (21), E136–E144.

Chen, L., Arambel, P.O., Mehra, R.K., 2002. Estimation under unknown correlation: Covariance intersection revisited. IEEE Trans. Autom. Control 47 (11), 1879–1882.

Chenouard, N., Bloch, I., Olivo-Marin, J.-C., 2013. Multiple hypothesis tracking for cluttered biological image sequences. IEEE Trans. Pattern Anal. Mach. Intell. 35 (11), 2736–2750.

Chenouard, N., Smal, I., De Chaumont, F., Maška, M., Sbalzarini, I.F., Gong, Y., Cardinale, J., Carthel, C., Coraluppi, S., Winter, M., Cohen, A.R., Godinez, W.J., Rohr, K., Kalaidzidis, Y., Liang, L., Duncan, J., Shen, H., Xu, Y., Magnusson, K.E., Jaldén, J., Blau, H.M., Paul-Gilloteaux, P., Roudot, P., Kervrann, C., Waharte, F., Tinevez, J.-Y., Shorte, S.L., Willemse, J., Celler, K., van Wezel, G.P., Dan, H.-W., Tsai, Y.-S., Ortiz de Solórzano, C., Olivo-Marin, J.-C., Meijering, E., 2014. Objective comparison of particle tracking methods. Nature Methods 11 (3), 281–290.

Coraluppi, S., Carthel, C., 2011. Multi-stage multiple-hypothesis tracking. J. Adv. Inf. Fusion 6 (1), 57–67.

Cox, I.J., 1993. A review of statistical data association techniques for motion correspondence. Int. J. Comput. Vis. 10 (1), 53–66.

de Chaumont, F., Dallongeville, S., Chenouard, N., Hervé, N., Pop, S., Provoost, T., Meas-Yedid, V., Pankajakshan, P., Lecomte, T., Le Montagner, Y., Lagache, T., Dufour, A., Olivo-Marin, J.-C., 2012. Icy: An open bioimage informatics platform for extended reproducible research. Nature Methods 9 (7), 690–696.

Deng, Z., Zhang, P., Qi, W., Liu, J., Gao, Y., 2012. Sequential covariance intersection fusion Kalman filter. Inform. Sci. 189, 293–309.

Dmitrieva, M., Zenner, H.L., Richens, J., St Johnston, D., Rittscher, J., 2019. Protein tracking by CNN-based candidate pruning and two-step linking with Bayesian network. In: Proc. IEEE International Workshop on Machine Learning for Signal Processing. IEEE, pp. 1–6.

Ewers, H., Smith, A.E., Sbalzarini, I.F., Lilie, H., Koumoutsakos, P., Helenius, A., 2005. Single-particle tracking of murine polyoma virus-like particles on live cells and artificial membranes. Proc. Natl. Acad. Sci. 102 (42), 15110–15115.

Fraser, D.C., Potter, J.E., 1969. The optimum linear smoother as a combination of two optimum linear filters. IEEE Trans. Autom. Control 14 (4), 387–390.

Genovesio, A., Liedl, T., Emiliani, V., Parak, W.J., Coppey-Moisan, M., Olivo-Marin, J.-C., 2006. Multiple particle tracking in 3-D+ t microscopy: Method and application to the tracking of endocytosed quantum dots. IEEE Trans. Image Process. 15 (5), 1062–1070.

Godinez, W.J., Lampe, M., Wörz, S., Müller, B., Eils, R., Rohr, K., 2009. Deterministic and probabilistic approaches for tracking virus particles in time-lapse fluorescence microscopy image sequences. Med. Image Anal. 13 (2), 325–342.

Godinez, W.J., Rohr, K., 2015. Tracking multiple particles in fluorescence time-lapse microscopy images via probabilistic data association. IEEE Trans. Med. Imaging 34 (2), 415–432.

Gudla, P.R., Nakayama, K., Pegoraro, G., Misteli, T., 2017. SpotLearn: Convolutional neural network for detection of fluorescence in situ hybridization (FISH) signals in high-throughput imaging approaches. In: Proc. CSH Symposia on Quant. Biol. 2017. CSH Laboratory Press, pp. 57–70.

Guo, Q., Chen, S., Leung, H., Liu, S., 2010. Covariance intersection based image fusion technique with application to pansharpening in remote sensing. Inform. Sci. 180 (18), 3434–3443.

Heun, P., Laroche, T., Shimada, K., Furrer, P., Gasser, S.M., 2001. Chromosome dynamics in the yeast interphase nucleus. Science 294 (5549), 2181–2186.

Imle, A., Kumberger, P., Schnellbächer, N.D., Fehr, J., Carrillo-Bustamante, P., Ales, J., Schmidt, P., Ritter, C., Godinez, W.J., Müller, B., Rohr, K., Hamprecht, F.A., Schwarz, U.S., Graw, F., Fackler, O.T., 2019. Experimental and computational analyses reveal that environmental restrictions shape HIV-1 spread in 3D cultures. Nature Commun. 10 (2144), 1–18.

Ivanchenko, S., Godinez, W.J., Lampe, M., Kräusslich, H.-G., Eils, R., Rohr, K., Bräuchle, C., Müller, B., Lamb, D.C., 2009. Dynamics of HIV-1 assembly and release. PLoS Pathog. 5 (11), 1–12.

Jaiswal, A., Godinez, W.J., Eils, R., Lehmann, M.J., Rohr, K., 2015. Tracking virus particles in fluorescence microscopy images using multi-scale detection and multi-frame association. IEEE Trans. Image Process. 24 (11), 4122–4136.

Jaqaman, K., Loerke, D., Mettlen, M., Kuwata, H., Grinstein, S., Schmid, S.L., Danuser, G., 2008. Robust single-particle tracking in live-cell time-lapse sequences. Nature Methods 5 (8), 695–702.

Julier, S.J., Uhlmann, J.K., 1997. A non-divergent estimation algorithm in the presence of unknown correlations. In: Proc. of the American Control Conference. IEEE, pp. 2369–2373.

Julier, S.J., Uhlmann, J.K., 2009. General decentralized data fusion with covariance intersection. In: Handbook of Multisensor Data Fusion: Theory and Practice. CRC Press.

Krawczyk, P., Borovski, T., Stap, J., Cijsouw, T., ten Cate, R., Medema, J.P., Kanaar, R., Franken, N., Aten, J., 2012. Chromatin mobility is increased at sites of DNA double-strand breaks. J. Cell Sci. 125 (9), 2127–2133.

Kuhn, H.W., 1955. The Hungarian method for the assignment problem. Nav. Res. Logist. Q. 2, 83–97.

Lee, J.-Y., Cortese, M., Haselmann, U., Tabata, K., Romero-Brey, I., Funaya, C., Schieber, N.L., Qiang, Y., Bartenschlager, M., Kallis, S., Ritter, C., Rohr, K., Schwab, Y., Ruggieri, A., Bartenschlager, R., 2019. Spatiotemporal coupling of the hepatitis C virus replication cycle by creating a lipid droplet-proximal membranous replication compartment. Cell Rep. 27 (12), 3602–3617.e5.

Levi, V., Gratton, E., 2008. Chromatin dynamics during interphase explored by single-particle tracking. Chromosom. Res. 16 (3), 439–449.

Liang, L., Shen, H., De Camilli, P., Duncan, J.S., 2014. A novel multiple hypothesis based particle tracking method for clathrin mediated endocytosis analysis using fluorescence microscopy. IEEE Trans. Image Process. 23 (4), 1844–1857.

Newby, J.M., Schaefer, A.M., Lee, P.T., Forest, M.G., Lai, S.K., 2018. Convolutional neural networks automate detection for tracking of submicron-scale particles in 2D and 3D. Proc. Natl. Acad. Sci. USA 115 (36), 9026–9031.

Niehsen, W., 2002. Information fusion based on fast covariance intersection filtering. In: Proc. IEEE International Conference on Information Fusion. IEEE, pp. 901–904.

Olivo-Marin, J.-C., 2002. Extraction of spots in biological images using multiscale products. Pattern Recognit. 35 (9), 1989–1996.

Pabba, M.K., Ritter, C., Chagin, V.O., Stear, J.H., Loerke, D., Kolobynina, K., Prorok, P., Schmid, A.K., Leonhardt, H., Rohr, K., Cardoso, M.C., 2023. Replisome loading reduces chromatin motion independent of DNA synthesis. eLife http://dx.doi.org/10.7554/eLife.87572.1.

Pan, K., Kokaram, A., Hillebrand, J., Ramaswami, M., 2010. Gaussian mixture models for spots in microscopy using a new split/merge EM algorithm. In: Proc. IEEE International Conference on Image Processing. IEEE, pp. 3645–3648.

Reinhardt, M., Noack, B., Arambel, P.O., Hanebeck, U.D., 2015. Minimum covariance bounds for the fusion under unknown correlations. IEEE Signal Process. Lett. 22 (9), 1210–1214.

Rezatofighi, S.H., Hartley, R., Hughes, W.E., 2012. A new approach for spot detection in total internal reflection fluorescence microscopy. In: Proc. IEEE International Symposium on Biomedical Imaging. IEEE, pp. 860–863.

Ritter, C., Imle, A., Lee, J.-Y., Müller, B., Fackler, O.T., Bartenschlager, R., Rohr, K., 2018. Two-filter probabilistic data association for tracking of virus particles in fluorescence microscopy images. In: Proc. IEEE International Symposium on Biomedical Imaging. IEEE, pp. 957–960.

Ritter, C., Wollmann, T., Lee, J.-Y., Imle, A., Müller, B., Fackler, O.T., Bartenschlager, R., Rohr, K., 2021. Data fusion and smoothing for probabilistic tracking of viral structures in fluorescence microscopy images. Med. Image Anal. 73, 102168.

Roudot, P., Ding, L., Jaqaman, K., Kervrann, C., Danuser, G., 2017. Piecewise-stationary motion modeling and iterative smoothing to track heterogeneous particle motions in dense environments. IEEE Trans. Image Process. 26 (11), 5395–5410.

Ruusuvuori, P., Äijö, T., Chowdhury, S., Garmendia-Torres, C., Selinummi, J., Birbaumer, M., Dudley, A.M., Pelkmans, L., Yli-Harja, O., 2010. Evaluation of methods for detection of fluorescence labeled subcellular objects in microscope images. BMC Bioinformatics 11 (248), 1–17.

Sage, D., Neumann, F.R., Hediger, F., Gasser, S.M., Unser, M., 2005. Automatic tracking of individual fluorescence particles: Application to the study of chromosome dynamics. IEEE Trans. Image Process. 14 (9), 1372–1383.

Särkkä, S., 2013. Bayesian Filtering and Smoothing. Cambridge University Press.

Sbalzarini, I.F., Koumoutsakos, P., 2005. Feature point tracking and trajectory analysis for video imaging in cell biology. J. Struct. Biol. 151 (2), 182–195.

Schneider, C.A., Rasband, W.S., Eliceiri, K.W., 2012. NIH image to ImageJ: 25 years of image analysis. Nature Methods 9 (7), 671–675.

Smal, I., Draegestein, K., Galjart, N., Niessen, W., Meijering, E., 2008a. Particle filtering for multiple object tracking in dynamic fluorescence microscopy images: Application to microtubule growth analysis. IEEE Trans. Med. Imaging 27 (6), 789–804.

Smal, I., Loog, M., Niessen, W., Meijering, E., 2010. Quantitative comparison of spot detection methods in fluorescence microscopy. IEEE Trans. Med. Imaging 29 (2), 282–301.

Smal, I., Niessen, W., Meijering, E., 2008b. A new detection scheme for multiple object tracking in fluorescence microscopy by joint probabilistic data association filtering. In: Proc. IEEE International Symposium on Biomedical Imaging. IEEE, pp. 264–267.

Spilger, R., Imle, A., Lee, J.-Y., Müller, B., Fackler, O.T., Bartenschlager, R., Rohr, K., 2020. A recurrent neural network for particle tracking in microscopy images using future information, track hypotheses, and multiple detections. IEEE Trans. Image Process. 29, 3681–3694.

Spilger, R., Lee, J.-Y., Chagin, V.O., Schermelleh, L., Cardoso, M.C., Bartenschlager, R., Rohr, K., 2021. Deep probabilistic tracking of particles in fluorescence microscopy images. Med. Image Anal. 72, 1–18.

Štěpka, K., Matula, P., Matula, P., Wörz, S., Rohr, K., Kozubek, M., 2015. Performance and sensitivity evaluation of 3D spot detection methods in confocal microscopy. Cytometry A 87 (8), 759–772.

Thomann, D., Rines, D.R., Sorger, P.K., Danuser, G., 2002. Automatic fluorescent tag detection in 3D with super-resolution: Application to the analysis of chromosome movement. J. Microsc. 208 (1), 49–64.

Tinevez, J.-Y., Perry, N., Schindelin, J., Hoopes, G.M., Reynolds, G.D., Laplantine, E., Bednarek, S.Y., Shorte, S.L., Eliceiri, K.W., 2017. TrackMate: An open and extensible platform for single-particle tracking. Methods 115, 80–90.

Vincent, L., 1993. Morphological grayscale reconstruction in image analysis: applications and efficient algorithms. IEEE Trans. Image Process. 2 (2), 176–201.

Wollmann, T., Ritter, C., Dohrke, J.-N., Lee, J.-Y., Bartenschlager, R., Rohr, K., 2019. DetNet: Deep neural network for particle detection in fluorescence microscopy images. In: Proc. IEEE International Symposium on Biomedical Imaging. pp. 517–520.

Xue, Q., Leake, M.C., 2009. A novel multiple particle tracking algorithm for noisy in vivo data by minimal path optimization within the spatio-temporal volume. In: Proc. IEEE International Symposium on Biomedical Imaging. IEEE, pp. 1158–1161.

Yao, Y., Smal, I., Grigoriev, I., Akhmanova, A., Meijering, E., 2020. Deep-learning method for data association in particle tracking. Bioinformatics 36 (19), 4935–4941.